

Article

# Mechanical and Thermal Properties of Low-Density $\text{Al}_{20+x}\text{Cr}_{20-x}\text{Mo}_{20-y}\text{Ti}_{20}\text{V}_{20+y}$ Alloys

Uttam Bhandari, Congyan Zhang and Shizhong Yang \* 

Department of Computer Science, Southern University and A&amp;M College, Baton Rouge, LA 70813, USA; uttam\_bhandari\_00@subr.edu (U.B.); congyan\_zhang@subr.edu (C.Z.)

\* Correspondence: shizhong\_yang@subr.edu

Received: 18 March 2020; Accepted: 2 April 2020; Published: 7 April 2020



**Abstract:** Refractory high-entropy alloys (RHEAs)  $\text{Al}_{20+x}\text{Cr}_{20-x}\text{Mo}_{20-y}\text{Ti}_{20}\text{V}_{20+y}$  ( $(x, y) = (0, 0), (0, 10),$  and  $(10, 15)$ ) were computationally studied to obtain a low density and a better mechanical property. The density functional theory (DFT) method was employed to compute the structural and mechanical properties of the alloys, based on a large unit cell model of randomly distributed elements. Debye–Grüneisen theory was used to study the thermal properties of  $\text{Al}_{20+x}\text{Cr}_{20-x}\text{Mo}_{20-y}\text{Ti}_{20}\text{V}_{20+y}$ . The phase diagram calculation shows that all three RHEAs have a single body-centered cubic (BCC) structure at high temperatures ranging from 1000 K to 2000 K. The RHEA  $\text{Al}_{30}\text{Cr}_{10}\text{Mo}_5\text{Ti}_{20}\text{V}_{35}$  has shown a low density of  $5.16 \text{ g/cm}^3$  and a hardness of 5.56 GPa. The studied RHEAs could be potential candidates for high-temperature application materials where high hardness, ductility, and low density are required.

**Keywords:** density functional theory; phase diagram; high-entropy alloy; mechanical and thermal properties

## 1. Introduction

The operating temperatures of aircraft engines and nuclear reactors are very high. Currently, most widely used alloys are nickel-based with working temperatures of 1200 K–1600 K. The performance of traditional nickel-based superalloys is thus limited to high-temperature applications ( $>1900 \text{ K}$ ), due to their low melting temperature and high density [1,2]. In past years, several high-temperature nickel-based superalloys such as Inconel 625 [3], SSR 99 [4], and Co–Ti–Cr [5] have been widely investigated. These reports show that while they have excellent mechanical properties, they also have high density. Ideally, the structural components of aircraft engines need low-density materials with high toughness and a high melting temperature, which motivates researchers in trying titanium-mixed refractory high-entropy alloys (RHEAs) [6–8]. RHEAs have attracted the interest of researchers due to their excellent mechanical property, high melting point, hardness, ductility, wear resistance, and high-temperature strength [9–12]. Studies on CrNbTiVZr [13], MoNbTaVW [14,15], and MoNbTaW [16] have shown that these RHEAs could be potential future candidate materials for high-temperature applications in aircraft engines and nuclear reactors. However, these RHEAs either have a relatively high density ( $>10 \text{ g/cm}^3$ ) or are brittle at room temperature, which limits their applications. Recently, Xu et al. [6] designed three RHEAs  $\text{Ti}_{50-x}\text{Al}_x\text{V}_{20}\text{Nb}_{20}\text{Mo}_{10}$  ( $x = 10, 15, 20$ ) with low densities ranging from  $6.01 \text{ g/cm}^3$  to  $5.876 \text{ g/cm}^3$ . These alloys have high strength and good plasticity at high temperatures. So far, Vickers hardness of these alloys has not been reported. Khaled group [7] also designed a low-density nanocrystalline high-entropy alloy  $\text{Al}_{20}\text{Li}_{20}\text{Mg}_{10}\text{Sc}_{20}\text{Ti}_{30}$  with a hardness of 5.9 GPa. However, this alloy has a low melting point which is not appropriate for high-temperature applications. Kang et al. [8] prepared an equimolar low-density RHEA AlCrMoTiV. They found a single body-centered cubic (BCC) phase in AlCrMoTiV using the X-ray diffraction (XRD) method. The measured Vickers hardness of AlCrMoTiV

is 5.54 GPa. No computer simulation is found on this RHEA AlCrMoTiV. The density and other physical properties of this alloy can be further tuned by optimizing the component concentration. It is highly desirable to develop a better RHEA based on this AlCrMoTiV, with a lower density, a higher melting point, and enhanced hardness and ductility.

The first-principles density functional theory (DFT) method was used to optimize the HEA AlCrMoTiV. We investigated a novel RHEA  $\text{Al}_{30}\text{Cr}_{10}\text{Mo}_5\text{Ti}_{20}\text{V}_{35}$  with the aim of decreasing the density for a more balanced mechanical property when compared to the previously discussed RHEAs. The molar percentages of Mo (10.28 g/cm<sup>3</sup>) and Cr (7.14 g/cm<sup>3</sup>) were reduced, as they both have high density. The molar percentages of the low-density elements V (6.11 g/cm<sup>3</sup>) and Al (2.7 g/cm<sup>3</sup>) were increased to ensure the low density of the alloy. As the melting point of Ti is lower than that of V, it was kept constant to keep the alloy highly solidus at high temperatures.

## 2. Computational Methods

Thermo-Calc 2019 software [17] was used to predict the phase equilibria of the RHEAs. The database used in this software was Thermo-Calc's high-entropy alloy (TCHEA1) database [18]. The phase prediction based on the TCHEA1 database was in good agreement with many experimental reports [19–22]. The first-principles method used in this study was based on DFT [23,24]. The computations were performed with the Vienna Ab initio Simulation Package (VASP 5.4) [25] as implemented in the MedeA software environment [26]. In this study, the electron-ion interactions were described by the projector augmented wave (PAW) [27]. The generalized gradient approximation (GGA) [28] of Perdew–Burke–Ernzerhof (PBE) [29] was used as an exchange-correlation function to optimize the structure. The BCC structure of the alloys was constructed with the help of the Knuth shuffle model [30] using Python code. The distribution of the component atoms was randomized in a 100-atom supercell model, which is shown in Figure 1a. To confirm the random distribution of the elements inside the supercell, we plotted the total and partial pair distribution functions (PDF) of the supercell, as shown in Figure 1b. In the BCC structure, each element had eight nearest adjacent elements, and six second nearest adjacent elements. In this case, there were a total of 400 pairs combined by the first adjacent elements, and 700 pairs by the second adjacent elements in the 100-atom supercell. In this supercell, there were 12 elements out of 400 pairs which were combined by the first nearest neighboring elements, and 22 elements out of 700 pairs were connected by the second nearest adjacent element. This demonstrates that the elements inside the supercell were uniformly distributed, providing an accurate high-entropy model.

The elastic constants were calculated using Le Page and Saxe's stress-strain method [31,32] on MedeA software. The stress tensor was calculated using analytic expressions. To ensure that the equilibrium structure corresponded to zero strain, the initial optimization of the theoretical cell parameters was made with high accuracy. The k-spacing was set as 0.2 per angstrom. Plane-wave cut-off energy of 500 eV was used. The geometry convergence criterion was set to 0.02 eV/Å, and the SCF convergence criterion to  $10 \times 10^{-5}$  eV. The k-mesh was forced to be centered on the gamma point. After calculating the elastic constant, the Voight–Reuss–Hill approximation [33,34] was used to calculate the mechanical properties of the RHEAs. The mathematical relations for calculating bulk modulus ( $B$ ), shear modulus ( $G$ ), Young's modulus ( $E$ ), and Poisson ratio ( $\nu$ ) are listed in the following equations:

$$B = \frac{1}{3}(C_{11} + 2C_{12}), G = \frac{1}{2}(G_{\text{Voight}} + G_{\text{Reuss}}) \quad (1)$$

where  $G_{\text{Voight}} = \frac{1}{5}(C_{11} - C_{12} + 3C_{44})$  and  $G_{\text{Reuss}} = \frac{5}{4(S_{11} - S_{12}) + 3S_{44}}$ ,  $S$  is compliance matrix,

$$E = \frac{9BG}{3B + G}, \text{ and } \nu = \frac{3B - 2G}{2(3B + G)}. \quad (2)$$

The thermodynamics calculations used in this study were based on the Debye theory [35]. In this theory, only the elastic constant and averaged Grüneisen constant values are needed to compute the thermal expansion coefficient for a cubic material. The Grüneisen constant ( $\gamma_G$ ) was derived from the pressure–volume equation by Mayer et al. [36]. The Debye temperature was computed by using the formula of the mean sound velocity ( $V_m$ ) as follows:

$$\theta_D = \frac{\hbar}{K} \left( \frac{6\pi^2 q}{V_0} \right)^{\frac{1}{3}} V_m \quad (3)$$

where  $q$  is the number of atoms in the unit cell,  $V_0$  its volume, and  $\hbar$  and  $K_B$  are Planck and Boltzmann constants, respectively. The lattice contribution to the specific heat capacity,  $C_V$ , as a function of temperature,  $T$ , was evaluated. The linear thermal expansion coefficient ( $\alpha$ ) was calculated using the relation in Reference 37 [36,37].

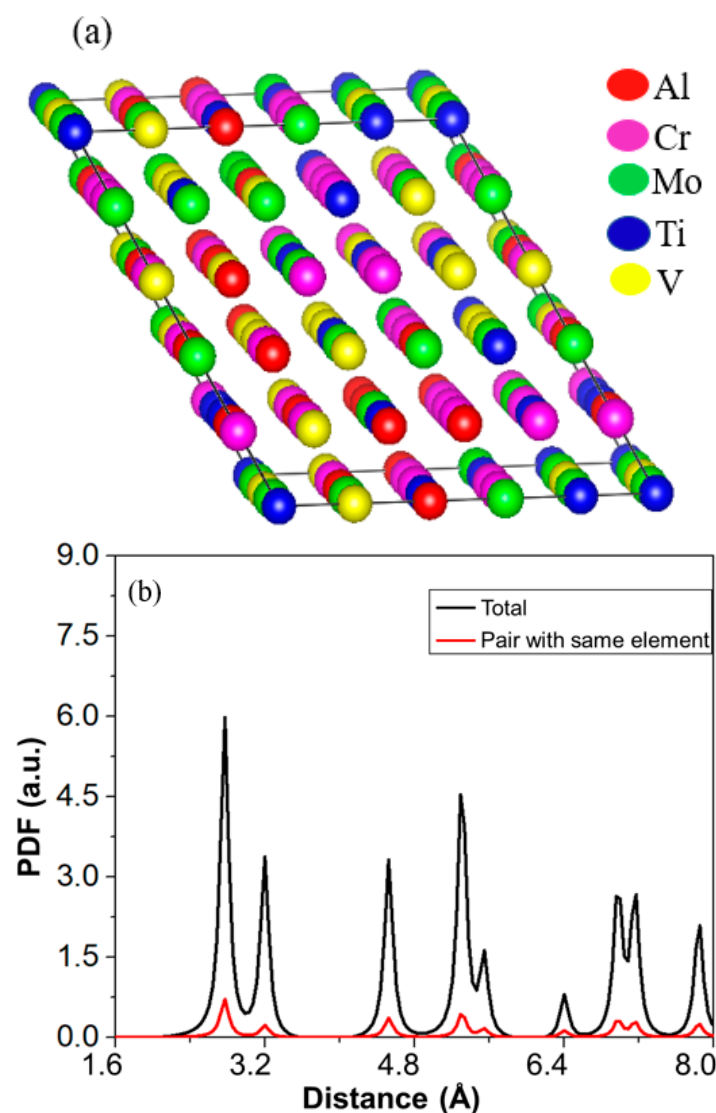


**Figure 1.** (a) Schematic of a random 100-atom unit cell model used for density functional theory (DFT) calculations. (b) Plot between total pair distribution function (PDF) of all pairs in the supercell and total PDF of pairs as a function of distance.

### 3. Results and Discussion

#### 3.1. Structural Properties

The phase formation and crystal structures of the design alloys were predicted by calculating the entropy of mixing ( $\Delta S_{mix}$ ) [38], mixing enthalpy ( $\Delta H_{mix}$ ) [39], atomic size differences ( $\delta$ ) [40], and valence electron concentration ( $VEC$ ) [41,42]. For the current RHEAs, corresponding values of  $\Delta S_{mix}$ ,  $\Delta H_{mix}$ ,  $VEC$ , and  $\delta$  were calculated using the following formula, and the results are listed in Table 1:

$$\Delta S_{mix} = -R \sum_{i=1}^n x_i \ln x_i \quad (4)$$

$$\Delta H_{mix} = 4 \times \sum_{i=1, i \neq j}^n \Delta H_{ij}^{mix} x_i x_j \quad (5)$$

$$\delta = 100 \times \sqrt{\sum_{i=1}^n c_i \left(1 - \frac{r_i}{\bar{r}}\right)^2}, \quad \bar{r} = \sum_{i=1}^n x_i r_i \quad (6)$$

$$VEC = \sum_{i=1}^n C_i (VEC)_i \quad (7)$$

where  $R$  is ideal gas constant,  $x_i$  and  $x_j$  are the atomic percentages of the  $i^{\text{th}}$  and  $j^{\text{th}}$  elements, respectively,  $r_i$  is the radius of the  $i^{\text{th}}$  element,  $\bar{r}$  is averaged atomic radius, and  $(VEC)_i$  is the valence electron concentration of the  $i^{\text{th}}$  element.

**Table 1.** Calculated values of entropy of mixing ( $\Delta S_{mix}$ ), mixing enthalpy ( $\Delta H_{mix}$ ), valence electron concentration ( $VEC$ ), and atomic size differences ( $\delta$ ) of the refractory high-entropy alloys (RHEAs).

Name of Alloys	$\Delta S_{mix}$ (J/K.mol)	$\Delta H_{mix}$ (kJ/mol)	$\delta$ (%)	$VEC$
Al <sub>20</sub> Cr <sub>20</sub> Mo <sub>20</sub> Ti <sub>20</sub> V <sub>20</sub>	13.38	−12.16	4.83	4.8
Al <sub>20</sub> Cr <sub>20</sub> Mo <sub>10</sub> Ti <sub>20</sub> V <sub>30</sub>	12.94	−13.04	4.92	4.7
Al <sub>30</sub> Cr <sub>10</sub> Mo <sub>5</sub> Ti <sub>20</sub> V <sub>35</sub>	11.89	−16.98	4.46	4.3

To form a solid solution, Zhang et al. [38] proposed that  $\Delta H_{mix}$  should be  $-15 \leq \Delta H_{mix} \leq 5$  kJ/mol, while Guo et al. [41] reported that  $\Delta H_{mix}$  should be  $-22 \leq \Delta H_{mix} \leq 7$  kJ/mol. These conditions were statistically calculated, and the data had some deviations in the previous findings [38,42–44]. Other criteria to form a stable solid solution are  $12 \leq \Delta S_{mix} \leq 17.5$  and  $\delta \leq 6.6\%$ . Another parameter to predict the crystal structure of HEAs is  $VEC$ . If  $VEC$  is  $\geq 8$ , the alloy will form a face-centered cubic (FCC) crystal, whereas if  $VEC$  is  $< 6.87$ , it will form a BCC crystal. Our calculated data in Table 1 show that the present RHEAs could form solid solutions with stable BCC crystal structures.

To provide more information on our initial structural prediction of the candidate alloys, the CALPHAD based Thermo-Calc software with the TCHEA1 database was employed to compute the phase diagram. The calculated equilibrium phase diagrams of the designed RHEAs are shown in Figure 2. The range of calculated temperature in the graph was from 900 K to 3000 K. As can be seen from the diagram, all the designed alloys keep the stable BCC phase at a high temperature of more than 2000 K, with no sign of phase transformation. According to the Thermo-Calc software, the melting point of Al<sub>20</sub>Cr<sub>20</sub>Mo<sub>20</sub>Ti<sub>20</sub>V<sub>20</sub>, Al<sub>20</sub>Cr<sub>20</sub>Mo<sub>10</sub>Ti<sub>20</sub>V<sub>30</sub>, and Al<sub>30</sub>Cr<sub>10</sub>Mo<sub>5</sub>Ti<sub>20</sub>V<sub>35</sub> were 2190 K, 2137 K, and 2025 K, respectively. The XRD patterns reported by Kang et al. [8] show the existence of a single BCC crystal structure in Al<sub>20</sub>Cr<sub>20</sub>Mo<sub>20</sub>Ti<sub>20</sub>V<sub>20</sub>. This experimental finding agrees with our prediction for Al<sub>20</sub>Cr<sub>20</sub>Mo<sub>20</sub>Ti<sub>20</sub>V<sub>20</sub>. Considering the experimental agreement and validation of the TCHEA1 database prediction according to a previous publication [19–22], we expect that future experimental results may confirm our phase prediction findings for Al<sub>20</sub>Cr<sub>20</sub>Mo<sub>10</sub>Ti<sub>20</sub>V<sub>30</sub> and Al<sub>30</sub>Cr<sub>10</sub>Mo<sub>5</sub>Ti<sub>20</sub>V<sub>35</sub>.

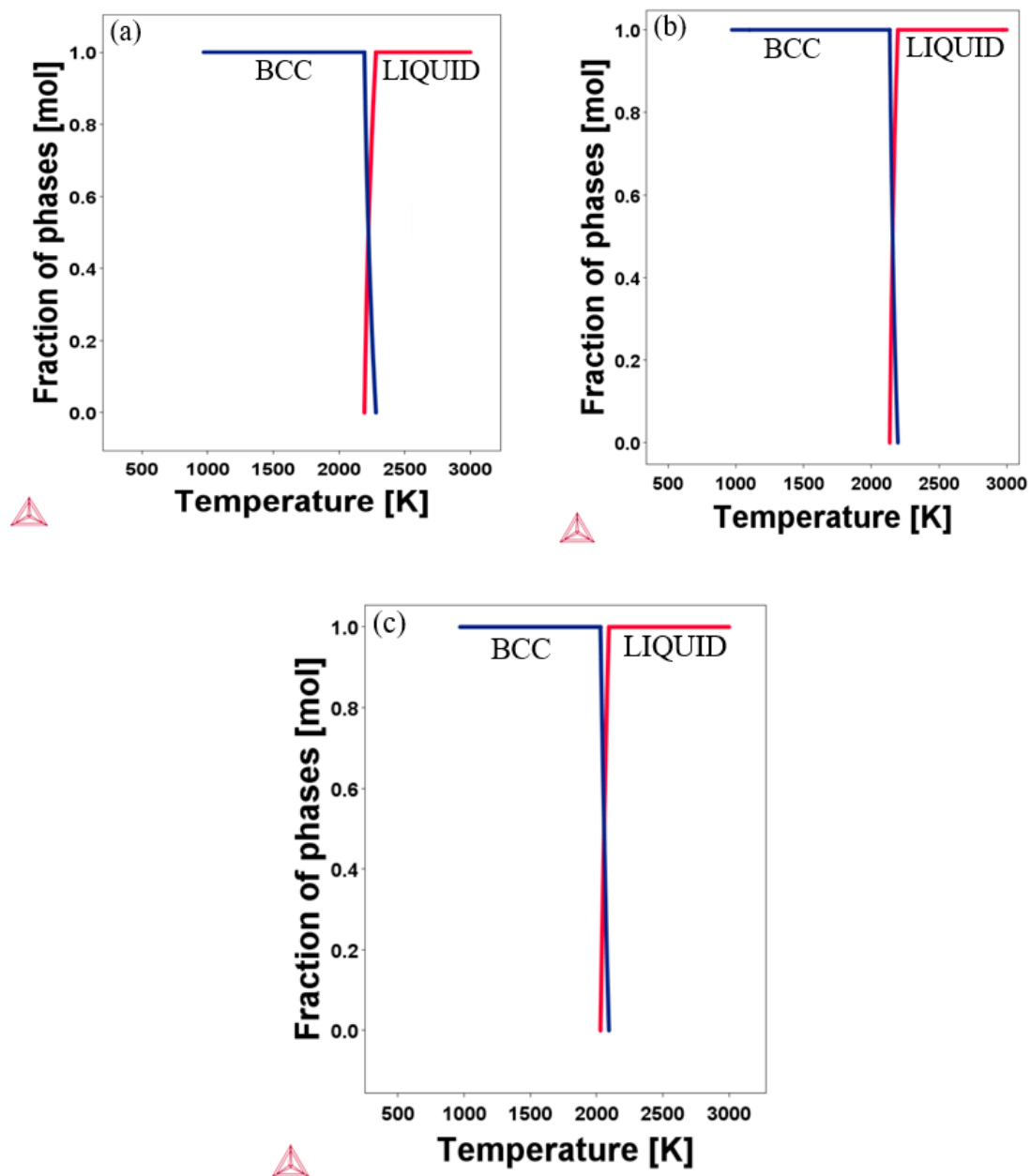


**Figure 2.** Calculated equilibrium phase diagrams of the RHEAs at high temperature: (a)  $\text{Al}_{20}\text{Cr}_{20}\text{Mo}_{20}\text{Ti}_{20}\text{V}_{20}$ ; (b)  $\text{Al}_{20}\text{Cr}_{20}\text{Mo}_{10}\text{Ti}_{20}\text{V}_{30}$ ; (c)  $\text{Al}_{30}\text{Cr}_{10}\text{Mo}_5\text{Ti}_{20}\text{V}_{35}$ .

### 3.2. Mechanical Properties

The structural optimization was performed with a supercell of 100 atoms to avoid the chance of lattice distortion among its constituent elements. The calculated elastic constants and other mechanical properties of the alloys are listed in Table 2. The optimized volumes of the 100-atoms models of  $\text{Al}_{20}\text{Cr}_{20}\text{Mo}_{20}\text{Ti}_{20}\text{V}_{20}$ ,  $\text{Al}_{20}\text{Cr}_{20}\text{Mo}_{10}\text{Ti}_{20}\text{V}_{30}$ , and  $\text{Al}_{30}\text{Cr}_{10}\text{Mo}_5\text{Ti}_{20}\text{V}_{35}$  were  $1447.42 \text{ \AA}^3$ ,  $1425.36 \text{ \AA}^3$ , and  $1461.51 \text{ \AA}^3$ , respectively. From these optimized volumes, lattice constants and densities were calculated. From the calculation,  $\text{Al}_{30}\text{Cr}_{10}\text{Mo}_5\text{Ti}_{20}\text{V}_{35}$  was found to have a low density of  $5.16 \text{ g/cm}^3$ .

**Table 2.** Calculated three independent elastic constants (GPa);  $C_{11}$ ;  $C_{12}$ ;  $C_{44}$ , Cauchy pressure  $C_{11}-C_{44}$  (GPa), bulk modulus  $B$  (GPa), shear modulus  $G$  (GPa), Young's modulus  $E$  (GPa), Poisson's ratio ( $\nu$ ), Pugh's ratio ( $B/G$ ), lattice constant  $a$  (Å), density  $\rho$  (gm/cm<sup>3</sup>) and hardness  $H_v$  (GPa) at zero pressure and Kelvin, respectively.

Alloys	$C_{11}$	$C_{12}$	$C_{44}$	$C_{11}-C_{44}$	$B$	$G$	$E$	$\nu$	$B/G$	$\rho$	$a$	$H_v$
Al <sub>20</sub> Cr <sub>20</sub> Mo <sub>20</sub> Ti <sub>20</sub> V <sub>20</sub>	255	119	69	186	165	61	163	0.33	2.72	6.28	3.07	5.48
Al <sub>20</sub> Cr <sub>20</sub> Mo <sub>10</sub> Ti <sub>20</sub> V <sub>30</sub>	247	111	64	183	157	60	161	0.32	2.62	5.85	3.05	5.66
Al <sub>30</sub> Cr <sub>10</sub> Mo <sub>5</sub> Ti <sub>20</sub> V <sub>35</sub>	246	90	63	183	143	56	149	0.32	2.71	5.16	3.08	5.56

The elastic constant of materials can yield information about their bonding and mechanical characteristics. All the given alloys satisfy the mechanically stable conditions as ( $C_{44} > 0$ ,  $C_{11} > |C_{12}|$ , and  $C_{11} + 2C_{12} > 0$ ) [45]. The ratio of bulk modulus ( $B$ ) to shear modulus ( $G$ ) can be used as an indicator to find the ductility in materials using the Pugh criterion [46]. The Pugh criterion states that a material with a  $B/G$  ratio greater than 1.75 behaves as ductile. The Poisson's ratio ( $\nu$ ) can be used as a descriptor for ductility. Gu et al. [47] reported that bulk metallic glasses with  $\nu > 31$  are very ductile. Moreover, the positive sign value of Cauchy pressure ( $C_{11} - C_{44}$ ) is associated with the metallic nature of polycrystalline material [48]. All three designed RHEAs show metallic nature, as all of them have a positive value of Cauchy pressure. Based on the computed outcomes of the Cauchy pressure, the Poisson ratio, and the Pugh criterion, we conclude that the designed RHEAs are ductile. The Vickers hardness ( $H_v$ ) of the designed alloy was calculated using Tian's model [49] as  $H_v = 0.92 \times K^{1.137} \times G^{0.708}$  where  $K = G/B$ . The calculated  $H_v$  of Al<sub>20</sub>Cr<sub>20</sub>Mo<sub>20</sub>Ti<sub>20</sub>V<sub>20</sub> is 5.48 GPa while the experimentally measured  $H_v$  value of Al<sub>20</sub>Cr<sub>20</sub>Mo<sub>20</sub>Ti<sub>20</sub>V<sub>20</sub> is 5.55 GPa [8]. The excellent agreement of calculated hardness with the experimental result confirms the reliability of our predicted value of bulk modulus and shear modulus. The excellent agreement of calculated hardness with the experimental result also confirms the reliability of our predicted value of elastic properties. The randomized model of the supercell used in our calculation may be used in predicting the mechanical and thermal properties of other future RHEAs. Our prediction may stimulate further experimental investigations of Al<sub>30</sub>Cr<sub>10</sub>Mo<sub>5</sub>V<sub>35</sub>Ti<sub>20</sub>, as it has a low density, is very ductile, and has a high melting point.

### 3.3. Thermal Properties

The thermal coefficient of linear expansion, alpha ( $\alpha$ ), as a function of temperature for Al<sub>20</sub>Cr<sub>20</sub>Mo<sub>20</sub>Ti<sub>20</sub>V<sub>20</sub>, Al<sub>20</sub>Cr<sub>20</sub>Mo<sub>10</sub>Ti<sub>20</sub>V<sub>30</sub> and Al<sub>30</sub>Cr<sub>10</sub>Mo<sub>5</sub>Ti<sub>20</sub>V<sub>35</sub> RHEAs is shown in Figure 3a. The calculated Debye temperature ( $\theta_D$ ) of Al<sub>20</sub>Cr<sub>20</sub>Mo<sub>20</sub>Ti<sub>20</sub>V<sub>20</sub>, Al<sub>20</sub>Cr<sub>20</sub>Mo<sub>10</sub>Ti<sub>20</sub>V<sub>30</sub>, and Al<sub>30</sub>Cr<sub>10</sub>Mo<sub>5</sub>Ti<sub>20</sub>V<sub>35</sub> were 428 K, 443 K, and 451 K, respectively. The higher value of  $\theta_D$  in materials reflects the strength of the covalent bond component in materials [50]. This reveals that the covalent bond component inside Al<sub>30</sub>Cr<sub>10</sub>Mo<sub>5</sub>Ti<sub>20</sub>V<sub>35</sub> could be stronger than the other two RHEAs, as it has a higher value of  $\theta_D$ . We found that the  $\alpha$  increases rapidly as temperature increases from 0 K to 200 K, and slowly becomes linear at temperatures above 600 K for the given RHEAs. The value of  $\alpha$  for Al<sub>30</sub>Cr<sub>10</sub>Mo<sub>5</sub>Ti<sub>20</sub>V<sub>35</sub> is similar to that of Al<sub>20</sub>Cr<sub>20</sub>Mo<sub>20</sub>Ti<sub>20</sub>V<sub>20</sub> and Al<sub>20</sub>Cr<sub>20</sub>Mo<sub>10</sub>Ti<sub>20</sub>V<sub>30</sub> at temperatures below 200 K, but its  $\alpha$  increases rapidly at temperatures above 298 K. This variation of the thermal coefficient of linear expansion indicates that the  $\alpha$  of Al<sub>30</sub>Cr<sub>10</sub>Mo<sub>5</sub>Ti<sub>20</sub>V<sub>35</sub> is very sensitive at temperatures above 298 K. It may be due to the addition of low-density elements such as Al and V in the RHEAs. Figure 3b shows the specific heat capacity at constant volume,  $C_v$ , as a function of temperature between Al<sub>20</sub>Cr<sub>20</sub>Mo<sub>20</sub>Ti<sub>20</sub>V<sub>20</sub>, Al<sub>20</sub>Cr<sub>20</sub>Mo<sub>10</sub>Ti<sub>20</sub>V<sub>30</sub>, and Al<sub>30</sub>Cr<sub>10</sub>Mo<sub>5</sub>Ti<sub>20</sub>V<sub>35</sub>. At low temperatures below 50 K, the  $C_v$  of all three RHEAs has identical behavior. At higher temperatures above 50 K, the  $C_v$  of Al<sub>30</sub>Cr<sub>10</sub>Mo<sub>5</sub>Ti<sub>20</sub>V<sub>35</sub>  $>$   $C_v$  of Al<sub>20</sub>Cr<sub>20</sub>Mo<sub>10</sub>Ti<sub>20</sub>V<sub>30</sub>  $>$   $C_v$  of Al<sub>20</sub>Cr<sub>20</sub>Mo<sub>20</sub>Ti<sub>20</sub>V<sub>20</sub>. This trend implies that the lowering of the high-density elements Mo and Cr increases the  $C_v$  of Al<sub>30</sub>Cr<sub>10</sub>Mo<sub>5</sub>Ti<sub>20</sub>V<sub>35</sub>. Since the specific heat capacity of Al<sub>30</sub>Cr<sub>10</sub>Mo<sub>5</sub>Ti<sub>20</sub>V<sub>35</sub> is higher, it can absorb more heat than the other

two RHEAs. We are not aware of the experimental report for the thermal properties of the present RHEAs, and future experiments will likely confirm our thermal properties results.

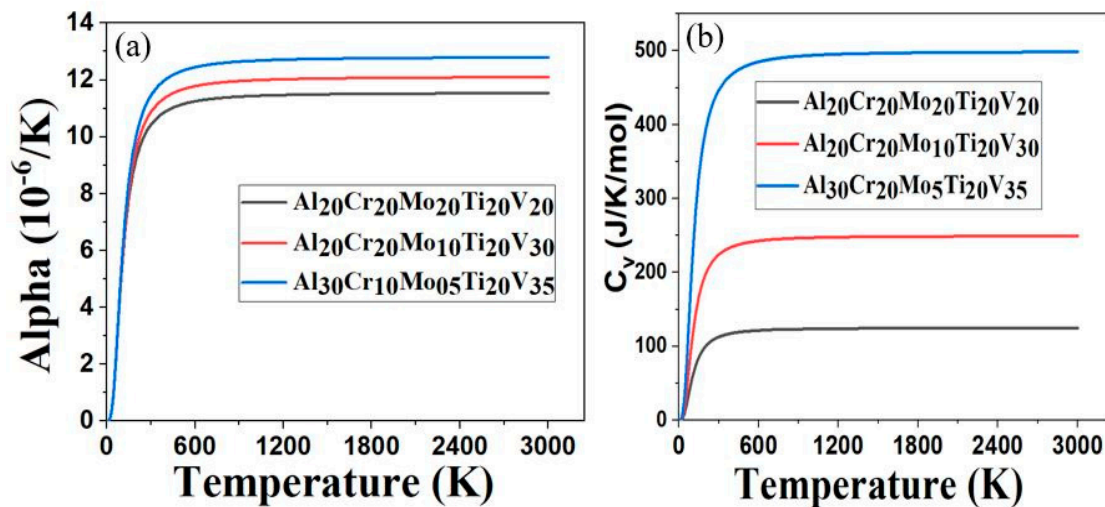


**Figure 3.** (a) Thermal coefficient of linear expansion as a function of temperature; (b) Specific heat capacity at constant volume as a function of temperature.

#### 4. Conclusions

Based on the first principles DFT calculation, CALPHAD method, and Debye theory method, structural, mechanical, and thermal properties of three RHEAs were studied. Novel  $\text{Al}_{30}\text{Cr}_{10}\text{Mo}_5\text{Ti}_{20}\text{V}_{35}$  RHEA has a low density of  $5.16 \text{ g/cm}^3$ , a hardness of 5.56 GPa, and maintains a stable BCC structure at high temperatures of 1000–2000 K. It also has a B/G ratio of 2.7, which indicates its ductile nature. Calculations of thermal properties show that the addition of elements Al and V increases the covalent bond component, thermal expansion coefficient, and the specific heat capacity of  $\text{Al}_{30}\text{Cr}_{10}\text{Mo}_5\text{Ti}_{20}\text{V}_{35}$  when compared with the previous RHEA  $\text{Al}_{20}\text{Cr}_{20}\text{Mo}_{20}\text{Ti}_{20}\text{V}_{20}$ . The present study reveals that based on structural and physical property calculations,  $\text{Al}_{30}\text{Cr}_{10}\text{Mo}_5\text{Ti}_{20}\text{V}_{35}$  could be a potential candidate for high-temperature applications. It is expected that further experimental exploration may validate our results on the structural, mechanical and thermal properties of these RHEAs.

**Author Contributions:** U.B. performed the computer simulation and wrote the original manuscript. C.Z. tested and verified 100 atom random unit cell model. U.B., C.Z. and S.Y. contributed to the discussion and writing. All authors have read and agreed to the published version of the manuscript.

**Funding:** This research is partially supported by the National Science Foundation (NSF) through the collaborative consortium CIMM and Department of Defense (DoD) through AFOSR.

**Acknowledgments:** This research is partially supported by NSF EPSCoR CIMM project under Award # OIA-1541079 and DoD support under contract W911NF1910005. The computational simulations were supported by the Louisiana Optical Network Infrastructure (LONI) with the supercomputer allocation loni\_mat\_bio12.

**Conflicts of Interest:** The authors declare no conflict of interest. The funders had no role in the design of the study; in the collection, analyses, or interpretation of data; in the writing of the manuscript, or in the decision to publish the results.

#### References

1. Perepezko, J.H. The Hotter the Engine, the Better. *Science* **2009**, *326*, 1068–1069. [[CrossRef](#)] [[PubMed](#)]
2. Pollock, T.M. Alloy design for aircraft engines. *Nat. Mater.* **2016**, *15*, 809–815. [[CrossRef](#)] [[PubMed](#)]
3. Albert, B.; Völkl, R.; Glatzel, U. High-temperature oxidation behavior of two nickel-based superalloys produced by metal injection molding for aero engine applications. *Metall. Mater. Trans. A* **2014**, *45*, 4561–4571. [[CrossRef](#)]

4. Kuhn, H.A.; Biermann, H.; Ungár, T.; Mughrabi, H. An X-ray study of creep-deformation induced changes of the lattice mismatch in the  $\gamma'$ -hardened monocrystalline nickel-base superalloy SRR 99. *Acta Metallurgica et Materialia* **1991**, *39*, 2783–2794. [CrossRef]
5. Zenk, C.H.; Povstugar, I.; Li, R.; Rinaldi, F.; Neumeier, S.; Raabe, D.; Göken, M. A novel type of Co–Ti–Cr-base  $\gamma/\gamma'$  superalloys with low mass density. *Acta Mater.* **2017**, *135*, 244–251. [CrossRef]
6. Xu, Z.Q.; Ma, Z.L.; Wang, M.; Chen, Y.W.; Tan, Y.D.; Cheng, X.W. Design of novel low-density refractory high entropy alloys for high-temperature applications. *Mater. Sci. Eng. A* **2019**, *755*, 318–322. [CrossRef]
7. Youssef, K.M.; Zaddach, A.J.; Niu, C.; Irving, D.L.; Koch, C.C. A Novel Low-Density, High-Hardness, High-entropy Alloy with Close-packed Single-phase Nanocrystalline Structures. *Mater. Res. Lett.* **2015**, *3*, 95–99. [CrossRef]
8. Kang, M.; Lim, K.R.; Won, J.W.; Lee, K.S.; Na, Y.S. Al-ti-containing lightweight high-entropy alloys for intermediate temperature applications. *Entropy* **2018**, *20*, 355. [CrossRef]
9. Li, C.; Li, J.C.; Zhao, M.; Jiang, Q. Effect of alloying elements on microstructure and properties of multiprincipal elements high-entropy alloys. *J. Alloy. Compd.* **2009**, *475*, 752–757. [CrossRef]
10. Zhang, Y. Mechanical properties and structures of high entropy alloys and bulk metallic glasses composites. *Mater. Sci. Forum* **2010**, *654*, 1058–1061. [CrossRef]
11. Zhou, Y.J.; Zhang, Y.; Wang, Y.L.; Chen, G.L. Solid solution alloys of AlCoCrFeNiTiX with excellent room-temperature mechanical properties. *Appl. Phys. Lett.* **2007**, *90*, 181904. [CrossRef]
12. Jung, C.; Kang, K.; Marshal, A.; Pradeep, K.G.; Seol, J.B.; Lee, H.M.; Choi, P.P. Effects of phase composition and elemental partitioning on soft magnetic properties of AlFeCoCrMn high entropy alloys. *Acta Mater.* **2009**, *171*, 31–39. [CrossRef]
13. Senkov, O.N.; Senkova, S.; Woodward, C.; Miracle, D.B. Low-density, refractory multi-principal element alloys of the Cr–Nb–Ti–V–Zr system: Microstructure and phase analysis. *Acta Mater.* **2013**, *61*, 1545–1557. [CrossRef]
14. Senkov, O.N.; Wilks, G.; Scott, J.; Miracle, D.B. Mechanical properties of Nb<sub>25</sub>Mo<sub>25</sub>Ta<sub>25</sub>W<sub>25</sub> and V<sub>20</sub>Nb<sub>20</sub>Mo<sub>20</sub>Ta<sub>20</sub>W<sub>20</sub> refractory high entropy alloys. *Intermetallics* **2011**, *19*, 698–706. [CrossRef]
15. Senkov, O.; Wilks, G.; Miracle, D.; Chuang, C.; Liaw, P. Refractory high-entropy alloys. *Intermetallics* **2010**, *18*, 1758–1765. [CrossRef]
16. Zou, Y.; Maiti, S.; Steurer, W.; Spolenak, R. Size-dependent plasticity in an Nb<sub>25</sub>Mo<sub>25</sub>Ta<sub>25</sub>W<sub>25</sub> refractory high-entropy alloy. *Acta Mater.* **2014**, *65*, 85–97. [CrossRef]
17. Thermo-Calc Software. Available online: <https://www.thermocalc.com/> (accessed on 7 April 2020).
18. Andersson, J.-O.; Helander, T.; Höglund, L.; Shi, P.; Sundman, B. Thermo-Calc & DICTRA, computational tools for materials science. *Calphad* **2002**, *26*, 273–312.
19. Lederer, Y.; Toher, C.; Vecchio, K.S.; Curtarolo, S. The search for high entropy alloys: A high-throughput ab-initio approach. *Acta Mater.* **2018**, *159*, 364–383. [CrossRef]
20. Chen, H.L.; Mao, H.; Chen, Q. Database development and Calphad calculations for high entropy alloys: Challenges, strategies, and tips. *Mater. Chem. Phys.* **2018**, *210*, 279–290. [CrossRef]
21. Mao, H.; Chen, H.L.; Chen, Q. TCHEA1: A thermodynamic database not limited for “high entropy” alloys. *J. Phase Equilibria Diffus.* **2017**, *38*, 353–368. [CrossRef]
22. Gao, M.C.; Zhang, B.; Yang, S.; Guo, S. Senary refractory high-entropy alloy HfNbTaTiVZr. *Metall. Mater. Trans. A* **2016**, *47*, 3333–3345. [CrossRef]
23. Hohenberg, P.; Kohn, W. Inhomogeneous electron gas. *Phys. Rev.* **1964**, *136*, B864. [CrossRef]
24. Kohn, W.; Sham, L.J. Self-Consistent Equations Including Exchange and Correlation Effects. *Phys. Rev.* **1965**, *140*, A1133–A1138. [CrossRef]
25. Kresse, G.; Furthmüller, J. Efficient iterative schemes for ab initio total-energy calculations using a plane-wave basis set. *Phys. Rev. B* **1996**, *54*, 11169–11186. [CrossRef] [PubMed]
26. MedeA<sup>®</sup> Software. Available online: <https://www.materialsdesign.com/medea-software> (accessed on 7 April 2020).
27. Blöchl, P.E. Projector augmented-wave method. *Phys. Rev. B* **1994**, *50*, 17953. [CrossRef] [PubMed]
28. Perdew, J.P.; Burke, K.; Ernzerhof, M. Generalized Gradient Approximation Made Simple. *Phys. Rev. Lett.* **1996**, *77*, 3865–3868. [CrossRef] [PubMed]
29. Monkhorst, H.J.; Pack, J.D. Special points for Brillouin-zone integrations. *Phys. Rev. B* **1976**, *13*, 5188. [CrossRef]
30. Knuth, E.D. *The Art of Computer Programming*, 3rd ed.; Addison-Wesley: Massachusetts, MA, USA, 1965.

31. Le Page, Y.; Saxe, P. Symmetry-general least-squares extraction of elastic coefficients from ab initio total energy calculations. *Phys. Rev. B* **2001**, *63*, 174103. [[CrossRef](#)]
32. Le Page, Y.; Saxe, P. Symmetry-general least-squares extraction of elastic data for strained materials from ab initio calculations of stress. *Phys. Rev. B* **2002**, *65*, 104104. [[CrossRef](#)]
33. Anderson, O.L. A simplified method for calculating the Debye temperature from elastic constants. *J. Phys. Chem. Solids* **1963**, *24*, 909–917. [[CrossRef](#)]
34. Andrews, K. Elastic moduli of polycrystalline cubic metals. *J. Phys. D: Appl. Phys.* **1978**, *11*, 2527. [[CrossRef](#)]
35. Grüneisen, E. *Zustand Thermische Eigenschaften der Stoffe*; Springer: Berlin, Germany, 1926.
36. Mayer, B.; Anton, H.; Bott, E.; Methfessel, M.; Sticht, J.; Harris, J.; Schmidt, P. Ab-initio calculation of the elastic constants and thermal expansion coefficients of Laves phases. *Intermetallics* **2003**, *11*, 23–32. [[CrossRef](#)]
37. Ashcroft, N.W.; Mermin, N.D. *Solid State Physics*; Holt-Saunders Int.: Philadelphia, PA, USA, 1976.
38. Zhang, Y.; Zhou, Y.J.; Lin, J.P.; Chen, G.L.; Liaw, P.K. Solid-solution phase formation rules for multi-component alloys. *Adv. Eng. Mater.* **2008**, *10*, 534–538. [[CrossRef](#)]
39. Takeuchi, A.; Inoue, A. Classification of bulk metallic glasses by atomic size difference, heat of mixing and period of constituent elements and its application to characterization of the main alloying element. *Mater. Trans.* **2005**, *46*, 2817–2829. [[CrossRef](#)]
40. Zhang, Y.; Zuo, T.T.; Tang, Z.; Gao, M.C.; Dahmen, K.A.; Liaw, P.K.; Lu, Z.P. Microstructures and properties of high-entropy alloys. *Prog. Mater. Sci.* **2014**, *61*, 1–93. [[CrossRef](#)]
41. Guo, S.; Ng, C.; Lu, J.; Liu, C. Effect of valence electron concentration on stability of fcc or bcc phase in high entropy alloys. *J. Appl. Phys.* **2011**, *109*, 103505. [[CrossRef](#)]
42. Wang, Z.; Huang, Y.; Yang, Y.; Wang, J.; Liu, C. Atomic-size effect and solid solubility of multicomponent alloys. *Scripta Materialia* **2015**, *94*, 28–31. [[CrossRef](#)]
43. Sheng, G.; Liu, C.T. Phase stability in high entropy alloys: Formation of solid-solution phase or amorphous phase. *Prog. Nat. Sci. Mater. Int.* **2011**, *21*, 433–446.
44. Yeh, J.W.; Chang, S.Y.; Hong, Y.D.; Chen, S.K.; Lin, S.J. Anomalous decrease in X-ray diffraction intensities of Cu-Ni-Al-Co-Cr-Fe-Si alloy systems with multi-principal elements. *Mater. Chem. Phys.* **2007**, *103*, 41–46. [[CrossRef](#)]
45. Wallace, D.C. *Thermodynamics of Crystals*; Wiley: Hoboken, NJ, USA, 1972.
46. Pugh, S. XCII. Relations between the elastic moduli and the plastic properties of polycrystalline pure metals. *Lond. Edinb. Dublin Philos. Mag. J. Sci.* **1954**, *45*, 823–843. [[CrossRef](#)]
47. Gu, X.; McDermott, A.; Poon, S.J.; Shiflet, G.J. Critical Poisson's ratio for plasticity in Fe-Mo-C-B-Ln bulk amorphous steel. *Appl. Phys. Lett.* **2006**, *88*, 211905. [[CrossRef](#)]
48. Nguyen-Manh, D.; Mrovec, M.; Fitzgerald, S.P. Dislocation driven problems in atomistic modelling of materials. *Mater. Trans.* **2008**, *49*, 2497–2506. [[CrossRef](#)]
49. Tian, Y.; Xu, B.; Zhao, Z. Microscopic theory of hardness and design of novel superhard crystals. *Int. J. Refract. Met. Hard Mater.* **2012**, *33*, 93–106. [[CrossRef](#)]
50. Wang, S.; Zhao, Y.; Hou, H.; Wen, Z.; Zhang, P.; Liang, J. Effect of anti-site point defects on the mechanical and thermodynamic properties of MgZn<sub>2</sub>, MgCu<sub>2</sub> Laves phases: A first-principle study. *J. Solid State Chem.* **2018**, *263*, 18–23. [[CrossRef](#)]

